



Synthesis of novel magnetic hydroxyapatite–biomass nanocomposite for arsenic and fluoride adsorption

V. N. Scheverin · E. M. Diaz · M. F. Horst ·
V. L. Lassalle

Received: 10 January 2024 / Accepted: 3 April 2024 / Published online: 2 May 2024
© The Author(s), under exclusive licence to Springer Nature B.V. 2024

Abstract A magnetic nanocomposite of hydroxyapatite and biomass (HAp–CM) was synthesized through a combined ultrasonic and hydrothermal method, aiming for efficient adsorption of arsenic (As) and fluoride (F^-) from drinking water in natural environments. The characterization of HAp–CM was carried out using TG, FTIR, XRD, SEM, SEM–EDS, and TEM techniques, along with the determination of pH_{pzc} charge. FTIR analysis suggested that coordinating links are the main interactions that allow the formation of the nanocomposite. XRD data indicated that the crystalline structure of the constituent materials remained unaffected during the formation of HAp–CM. SEM–EDS analysis revealed a Ca/P molar ratio of 1.78. Adsorption assays conducted in batches demonstrated that As and F^- followed a PSO kinetic model. Furthermore, As adsorption fitting well

to the Langmuir model, while F^- adsorption could be explained by both Langmuir and Freundlich models. The maximum adsorption capacity of HAp–CM was found to be 5.0 mg g^{-1} for As and 10.2 mg g^{-1} for F^- . The influence of sorbent dosage, pH, and the presence of coexisting species on adsorption capacity was explored. The pH significantly affected the nanocomposite's efficiency in removing both pollutants. The presence of various coexisting species had different effects on F^- removal efficiency, while As adsorption efficiency was generally enhanced, except in the case of PO_4^{3-} . The competitive adsorption between F^- and As on HAp–CM was also examined. The achieved results demonstrate that HAp–CM has great potential for use in a natural environment, particularly in groundwater remediation as a preliminary treatment for water consumption.

Supplementary Information The online version contains supplementary material available at <https://doi.org/10.1007/s10653-024-01981-w>.

V. N. Scheverin (✉) · E. M. Diaz · M. F. Horst ·
V. L. Lassalle
Instituto de Química del Sur (INQUISUR), CONICET/
UNS, CCT-BB, Av. Alem 1253, B8000 Bahía Blanca,
Buenos Aires, Argentina
e-mail: veronica.scheverin@uns.edu.ar

V. N. Scheverin · M. F. Horst · V. L. Lassalle
Departamento de Química, Universidad Nacional del
Sur (UNS), Av. Alem 1253, B8000 Bahía Blanca,
Buenos Aires, Argentina

Keywords Water treatment · Groundwater ·
Adsorption · Hydroxyapatite · Biomass · Magnetite ·
Arsenic · Fluoride · Nanocomposite

Introduction

Groundwater plays a crucial role in social development, particularly in arid and semiarid rural regions where access to surface water is limited or insufficient. This resource is vital for the livelihoods of 2.5 billion people worldwide, being essential in rural areas to meet fundamental needs such as

providing drinking water, irrigation, and supporting livestock (WWAP, 2019). Given the substantial reliance of the population on groundwater, its contamination has evolved into a pressing global concern. Arsenic (As) and fluoride (F^-) emerge as two significant natural pollutants in groundwater. Prolonged exposure to arsenic or fluoride from drinking water can lead to severe health issues, including various arsenic-related diseases such as cancers and skeletal fluorosis (World Health Organization, 2011).

Approximately 140–200 million people worldwide face chronic exposure to elevated concentrations of arsenic and fluoride, respectively. The co-occurrence of these contaminants has been extensively and globally documented, given their common sources and mobilization mechanisms (Alarcón-Herrera et al., 2013; Kumar et al., 2016, 2020). The most affected Countries by the simultaneous presence of both contaminants in groundwater include Pakistan, India, China, Mexico, and Argentina (Kumar et al., 2020). Specifically, in our country (Argentina), this phenomenon could be found in a great extension of the territory being dominant in the Chaco-Pampean plain. This is the region housing the country's major aquifers (Nicolli et al., 2012). Within this area, As and F^- levels in groundwater have been recorded reaching up to 5 mg L^{-1} and 18 mg L^{-1} , respectively, depending on depth and climatic variations (Al Rawahi, 2016; Alarcón-Herrera et al., 2013; Paoloni et al., 2003). Notably, the coexistence of both contaminants significantly increases health risks (Kumar et al., 2020). Simultaneous exposure to As and F^- has more severe genotoxic effects compared to isolated exposure to each pollutant, particularly impacting the nervous system, especially among children, resulting in decreased coefficient levels of intellectual and functional capabilities (Kumar et al., 2020; Rocha Amador, 2005; Zeng et al., 2014). Considering these elements' health impacts, the World Health Organization (WHO) provided a guideline value of 0.010 mg L^{-1} for arsenic and 1.50 mg L^{-1} for fluoride (World Health Organization, 2011).

Various methodologies have been developed for water treatment; however, their practical application faces limitations due to several factors. The intricate composition of natural water matrices plays a crucial role in determining the feasibility of different treatments. The success of treatment relies on key

parameters including pH, contaminant concentration, redox conditions, and the presence of coexisting species.

Numerous methodologies have been developed for water treatment. However, their implementation in the field is limited by several factors. For example, the complex composition of natural water matrices is a determining factor in applying different treatments. In this sense, the success of the treatment will depend on parameters such as pH, contaminant concentration, redox conditions, and the presence of coexisting species. Additionally, other factors related to the sustainability of the proposed procedures must be considered, such as the reusability of the technology, final disposal, and the treatment of the waste it generates (if any). In this regard, economic factors should be further considered in the choice of technology, since the environments where it would be implemented are generally rural or sparsely populated areas lacking common facilities (Litter et al., 2010).

Membrane filtration, ion exchange, precipitation, coagulation, permeable reactive barriers and adsorption are the most commonly applied methodologies for arsenic and fluoride removal from groundwater (Maity et al., 2021). Among these methodologies, the adsorption process is considered simple and relatively inexpensive, which makes it particularly suitable for application in small communities or rural areas. In general, commonly employed adsorbents include alumina, activated carbon, calcium-based adsorbents, zero-valent iron, and iron oxides (Habuda-Stanić et al., 2014; Hao et al., 2018). In this context, calcium-based materials can simultaneously retain various pollutants, including arsenic and fluoride (Pai et al., 2020).

Hydroxyapatite (HAp; $\text{Ca}_{10}(\text{PO}_4)_6(\text{OH})_2$), is a naturally occurring mineral known for its high insolubility, biocompatibility, and non-toxicity. Due to its ion exchange capacity and physicochemical properties, HAp exhibits a remarkable capacity to adsorb several contaminants, particularly fluorides (Gómez Hortigüela et al., 2014). Although HAp nanoparticles have shown promise in removing fluoride, their tendency to aggregate in water reduces the efficiency of the process (Jung et al., 2019). One way to prevent agglomeration involves the development of hydroxyapatite-based nanocomposites. Researchers have investigated the synthesis of nanocomposites using different materials, such as biochar (Jung et al.,

2019), biopolymers (Yang et al., 2016a, 2016b) and biomass from various sources (Zhang et al., 2016). Furthermore, it has been suggested that hydroxyapatite-based nanocomposites can enhance stability by reducing component leaching through adsorption mechanisms (Yang et al., 2016a, 2016b).

In this context, in our previous work, we successfully synthesized a hydroxyapatite–biomass nanocomposite (HAp–C) through hydrothermal synthesis and evaluated its fluoride removal capacity (Scheverin et al., 2022a). The HAp–C nanocomposite exhibited improved stability and efficiency in fluoride removal regarding HAp nanoparticles. Hap-C exhibited significant potential for removal arsenic and fluoride from groundwater samples. However, competition for active sites hindered the simultaneous removal of both contaminants.

Several studies have demonstrated that incorporating iron-based moieties into materials, such as hydroxyapatite and zeolites, can enhance their arsenic adsorption capacity (Pizarro et al., 2015; Scheverin et al., 2022b; Yang et al., 2022). For example, Panchu et al. (2022) conducted a study to evaluate the adsorption capacity of As^{3+} in hydroxyapatite (HAp) and its iron-doped variant (Fe–HAp) at low concentrations ($\leq 50 \mu\text{g L}^{-1}$). The results revealed that Fe–HAp exhibited a 32% higher adsorption capacity for As^{3+} compared to HAp. Furthermore, Fe–HAp demonstrated a significantly higher adsorption rate, being 538% faster than hydroxyapatite. It is noteworthy that Fe–HAp also displayed notable reusability efficiency, maintaining its adsorption capacity over 7 consecutive cycles. In a similar study, Khatamian et al., (2023) compared the arsenic adsorption capacity of zeolite A with $\text{Fe}_3\text{O}_4/\text{zeolite A}$ and $\text{Fe}_2\text{O}_3/\text{zeolite A}$ nanocomposites. The results highlighted a significant enhancement in arsenic adsorption capacity upon synthesizing iron oxide nanoparticles onto zeolite A.

Various methods have been reported for synthesizing hydroxyapatite–magnetite nanocomposites, including sol–gel methodology, hydrothermal synthesis, co-precipitation, and sonochemical methods (Biedrzycka et al., 2021). Hydrothermal synthesis stands out among these methods due to its simplicity, low cost, and compatibility with other synthesis techniques, such as co-precipitation (Kermanian et al., 2020; Zheltova et al., 2020).

This research aims to synthesize a hybrid hydroxyapatite–biomass–magnetite nanocomposite

(HAp–CM) to be employed as an adsorbent to remove arsenic and fluoride from groundwater sources. To achieve this, biomass of vegetal origin was used as a carbonaceous biomass source. The magnetic hydroxyapatite–biomass nanocomposite was synthesized using a combined ultrasonic/hydrothermal method. This study encompasses a comprehensive analysis of the physicochemical properties of the prepared nanocomposite, coupled with the evaluation of its performance in As and F^- removal. Various physicochemical parameters, such as contact time, initial fluoride concentration, dosage, pH, and the presence of coexisting species, were investigated for each pollutant. Furthermore, the adsorption efficiency of the nanocomposite was assessed using a natural groundwater sample.

A literature review revealed that the synthesis and application of the nanocomposite material discussed in this work have not been previously reported. While there are a few studies mentioning the obtention of hydroxyapatite–biomass nanocomposites based on different starting materials, the significant contribution of this work lies in the opportunity to explore the performance of this material within the complexity of natural water sources. This study presents a unique and more realistic approach to evaluating the effectiveness of the synthesized material in removing As and fluoride F^- from groundwater samples.

Experimental

Materials

The sunflower husk (C) employed in this work was collected from oilseed industry, Bahía Blanca, Argentina. For the synthesis of the composite material C was previously ground and sieved to obtain 297 μm particle size. All chemical reagents were of analytical grade and were used without further purification. Calcium nitrate tetrahydrate and Ammonium phosphate monobasic were provided by Sigma-Aldrich. Ferrous sulphate heptahydrate was provided by Mallinckrodt Chemical Works (USA) and Ferric chloride hexahydrate was provided by Tetrahedron. Sodium hydroxide was purchased from Cicarelli (Argentina).

Methods

Synthesis of magnetic hydroxyapatite–biomass composite

Magnetic hydroxyapatite–biomass nanocomposite (HAp–CM) was synthesized by hydrothermal method, using a nominal HAp:C:M ratio of 4:1:1 (w:w:w). The method included the preparation of two dispersions: (i) HAp–C, and (ii) M prior to hydrothermal treatment.

In the '(i) HAp–C' dispersion, the biomass was mixed with a calcium nitrate solution, and subsequently, $\text{NH}_4\text{H}_2\text{PO}_4$ was introduced, following the procedure outlined in our prior work (Scheverin et al., 2022a). Meanwhile, the '(ii) M' dispersion was obtained from a solution of $\text{Fe}^{2+}/\text{Fe}^{3+}$ in a 2:1 molar ratio.

Following preparation, the '(i) HAp–C' and '(ii) M' dispersions were combined and transferred into a hydrothermal reactor. The resulting black solid was isolated using a magnet and subjected to multiple washes with distilled water until the supernatant displayed low conductivity ($\leq 50 \mu\text{S cm}^{-1}$). Subsequently, the solid material was dried at 40°C for 48 h.

Characterization

Thermogravimetric analyses (TG) were performed using a TGA Q500 V20.13 Build 39 instrument. Tests were run from 30°C to 800°C at a heating rate of $10^\circ\text{C}/\text{min}$ under an N_2 atmosphere. Fourier transform infrared (FTIR) spectra were taken using a Thermo Scientific Nicolet iS50 covering the $4000\text{--}400 \text{ cm}^{-1}$ range. For this purpose, 1 mg of sample was ground with 250 mg of anhydrous KBr and compressed into a pellet used for the spectrum collection. X-ray diffraction (XRD) patterns were recorded by a PANalytical Empyrean 3 diffractometer with Ni filtered $\text{CuK}\alpha$ radiation, a graphite monochromator, and a PIXcel3D detector. It was operated at a voltage of 45 kV and a current of 40 mA, in the 2Θ range from 5° to 70° using a continuous scan mode with a scan angular speed of $0.016^\circ/\text{min}$. An estimation of the crystallite size of hydroxyapatite

$$D = \frac{K\lambda}{\beta\cos\theta} \quad (1)$$

where D is the crystal size (nm); K is the shape factor, usually taken as 0.89 for ceramic materials; λ is

the X-ray wavelength (nm); θ is the Bragg's angle, and β is the full width at half-maximum (FWHM) of the strongest peak of hydroxyapatite (2 1 1), and magnetite (3 1 1).

Scanning electron microscopy (SEM) and energy dispersive X-ray spectroscopy (EDS) were performed using a JEOL 35CF (Tokio, Japan 1983). The sample were covered with a gold layer for take the SEM micrographs, while for EDS analysis were covered with graphite. The EDS compositional estimation was considered the average of three scanning regions. Transmission electron microscopy (TEM) images were captured using a JEOL 100 CX II (JEOL, Tokyo, Japan 1983).

The pH of the point of zero charge (pH_{pzc}) of the materials was measured using the pH drift method (Newcombe et al., 1993). First, the pH of the solutions was adjusted between 5 and 9 by adding either HCl or NaOH, using 0.01 M NaCl as electrolyte support. Then, the adsorbent introduced into each solution at a ratio of 4 mg mL^{-1} ratio. Following a stabilization period of 24 h, during which the pH of the solutions had reached equilibrium, the final pH was recorded. The determination of pH_{pzc} involved plotting the curve of ΔpH ($\text{pH}_f - \text{pH}_i$) against pH_i and identifying the intersection point.

Batch adsorption assays

The adsorption tests were carried out to study the efficiency of HAp–CM for the removal of arsenic and fluoride in aqueous media. For this purpose, the removal capacity of each pollutant was first studied separately under different experimental conditions. All the experiments were carried out by the batch method using an orbital shaker (50 rpm) at room temperature. Standard solutions of HCl and NaOH (0.01 M) were employed for pH adjustment. Except for the pH effect experiment, the pH of the working solutions was controlled at 6 ± 0.2 . After each experiment, the solids were separated by a magnetic field and passed through a $0.45 \mu\text{m}$ syringe filter. The residual fluoride concentration in the treated samples was quantified employing a fluoride ion-selective electrode. On the other hand, the content of total As was measured by inductively coupled plasma atomic emission spectroscopy (ICP-AES Shimadzu 1000 mod III) or a furnace using a spectrophotometric

method (Murphy and Riley, 1962) according to their concentration level.

The adsorption kinetics experiments were carried out using a 10 mg L⁻¹ As or 6 mg L⁻¹ F⁻ solutions, with an adsorbent dose of 1 g L⁻¹. Based on these results, the optimum contact times for arsenic and fluoride adsorption were selected at 60 and 150 min, for further testing. Additionally, to evaluate the kinetic mechanism of As and F⁻ adsorption, three kinetic models were applied: pseudo-first-order (PFO), pseudo-second-order (PSO) and Weber-Morris kinetic models. Details of the kinetic models are included in supplementary material (S.1.1).

Adsorption isotherm studies were performed with initial concentrations of the contaminants ranged from 1 to 60 mg L⁻¹ for As or 1–35 mg L⁻¹ for F⁻. The adsorbent dose used was 1 g L⁻¹ for both contaminants. The Langmuir and Freundlich isotherm models were used to describe the adsorption process. The description of the isotherm models and fitting criteria used can be found in supplementary material (S.1.2).

The effect of adsorbent dosage, pH variation, and the presence of coexisting species was tested using 10 mg L⁻¹ of As and 6 mg L⁻¹ of F⁻ as initial concentrations. The adsorbent dose was studied varying the amount of material from 1 to 4 g L⁻¹.

The effect of the pH on the As and F⁻ adsorption was studied by adjusting the pH from 4.5 to 8.5, using an adsorbent dose of 4 g L⁻¹. The influence of coexisting ions (Cl⁻, HCO₃⁻, NO₃⁻, SO₄²⁻, PO₄³⁻, and Ca²⁺) on adsorption efficiency was explored. For this purpose, different solutions were prepared from the sodium salts to contain 250 mg L⁻¹ of selected coexisting species, adjusting the pH of the solution to 8.5. Additionally, the competitive adsorption between As and F⁻ was studied. Low (0.250 mg L⁻¹) and high (10 mg L⁻¹) arsenic concentration with a fluoride concentration of 6 mg L⁻¹ were studied.

All the experiments were conducted in triplicate, using the means and standard deviations of the results for data analysis. The removal efficiency (%R) and equilibrium adsorbed concentration (Q_e; mg g⁻¹) were calculated according to the following equations:

$$\%R = \frac{(C_i - C_f) \times 100\%}{C_i} \tag{2}$$

$$Q_e = \frac{(C_i - C_f) \times V}{M} \tag{3}$$

where C_i and C_f are the initial and final concentration of As or F⁻ (mg L⁻¹), V is the total volume of solution (L) and M is de adsorbent mass (g).

Natural water assays

The groundwater sample used for adsorption assays was collected from the General Alvear district in Mendoza, Argentina. In this geographic area, the groundwater resource presents high conductivity and salinity. This groundwater resource exhibits high conductivity and salinity levels, as detailed in Table 1. It is important to note that the concentration of As and F⁻ in these waters is low. Therefore, the matrix was enriched with both contaminants. The pH was left unregulated for the experiments, and the sample was not subjected to filtration.

The effectiveness of HAp–CM in adsorbing As and F⁻ from groundwater was evaluated through five successive adsorption cycles, with no purification or regeneration steps implemented between cycles.

Table 1 Chemical composition of groundwater used for natural water assays

| Parameter | Value | Unit |
|--|-------|--------------------------------------|
| F ⁻ | 3.06 | mg L ⁻¹ |
| As | 0.116 | mg L ⁻¹ |
| Fe | 0.142 | mg L ⁻¹ |
| Na | 498 | mg L ⁻¹ |
| Ca | 70.7 | mg L ⁻¹ |
| Mg | < 1 | mg L ⁻¹ |
| Cl ⁻ | 199.6 | mg L ⁻¹ |
| pH | 7.80 | |
| Conductivity | 1902 | μS cm ⁻¹ |
| Total dissolved solids | 1.35 | ppt |
| Salinity | 0.95 | ppt |
| Total Hardness | 7.08 | mg CaCO ₃ L ⁻¹ |
| Total alkalinity | 527.2 | mg CaCO ₃ L ⁻¹ |
| HCO ₃ ⁻ alkalinity | 496.0 | mg CaCO ₃ L ⁻¹ |
| CO ₃ ²⁻ alkalinity | 31.06 | mg CaCO ₃ L ⁻¹ |

Results and discussion

Characterization of the adsorbent synthesized

Thermogravimetric analysis

Thermogravimetric analysis (TGA) was employed to estimate the composition of the nanocomposite concerning the percentage of its organic and inorganic phases. Figure 1 shows the thermogravimetric profile of HAp–CM nanocomposite. As can be seen, the magnetic nanocomposite shows three different weight-loss regions. The first drop-in weight of about 8.5% is registered for temperatures below 250 °C. This drop-in weight is due to the release of moisture and some light volatiles. Weight loss in the range of 250–550 °C may be associated with the thermal decomposition of cellulose, hemicellulose, and primary pyrolysis of lignin that compose the biomass (Burhenne et al., 2013). A third weight drop of 8.5% is registered for temperatures beyond 550 °C; and it is usually linked with secondary pyrolysis of lignin-forming biochar residue (Mishra & Mohanty, 2018; Salema et al., 2019). We obtained similar results for magnetic nanocomposite precursors (Scheverin et al., 2022a).

Then, the thermogravimetric analysis's data reveals that HAp–CM undergoes a total weight loss of about 22.9%. This percentage is attributed to both water (8.5%) and biomass (13.6%) content. The latter falls short of the theoretical nominal value (16.6%).

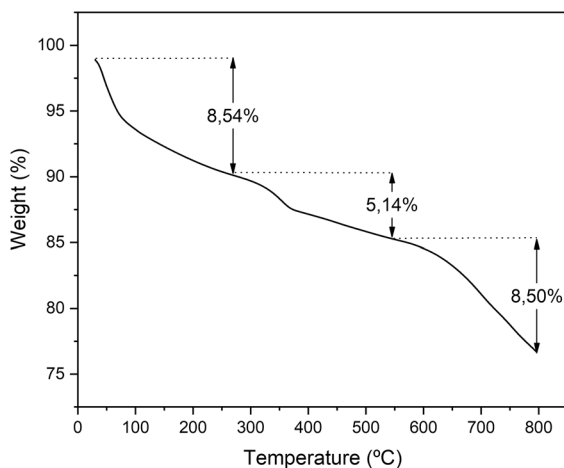


Fig. 1 Thermogravimetric profile of HAp–CM

Additionally, these results estimate the percentage of inorganic phases (hydroxyapatite and magnetite) in the nanocomposite to be approximately 77.8%, also less than the nominal value.

FTIR spectroscopy

FTIR spectroscopy was used to evaluate the presence of exposed functional groups and to infer the possible binding interactions leading to the formation of the HAp–CM composite. The FTIR spectra of the magnetic composite (Fig. 2) show signals assigned to the hydroxyapatite structure's four types of vibrational modes of phosphate (PO_4^{3-}). The triply degenerated asymmetric stretching mode (ν_3 P–O) is observed as an intense band at 1043 cm^{-1} , accompanied by a weak shoulder at 1096 cm^{-1} . The symmetric stretching mode (ν_1 P–O) appears as a sharp peak at 963 cm^{-1} . Additionally, bands observed within the $700\text{--}500\text{ cm}^{-1}$ and $490\text{--}450\text{ cm}^{-1}$ ranges may correspond to the triply degenerate in-plane bending mode (ν_4 O–P–O) and doubly degenerate out-of-plane bending mode (ν_2 O–P–O), respectively (REHMAN & BONFIELD, 1997).

Bands located between 1540 and 1300 cm^{-1} might be associated with the presence of CO_3^{2-} in the structure of the nanocomposite. The presence of carbonate could be explained by considering the synthesis condition. In this sense, under high alkalinity conditions, the OH^- ions present in the medium can react with the atmospheric CO_2 ,

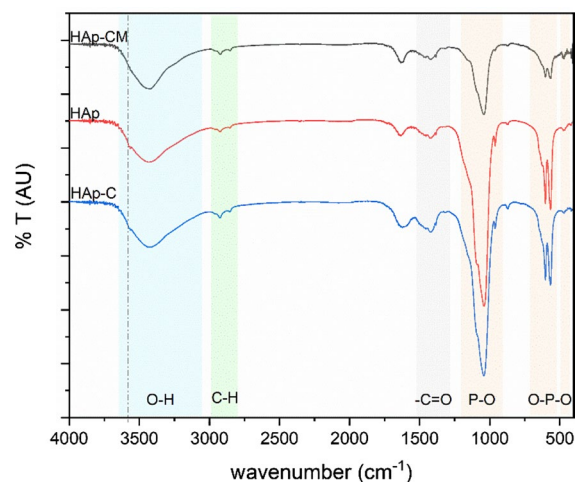


Fig. 2 FTIR spectra of HAp–CM

increasing the CO_3^{2-} concentration in the synthesis solution causing a partial replacement of phosphate or hydroxyl groups of HAp–CM with CO_3^{2-} . This observation agrees with the results of previous investigations, where we found that hydroxyapatite synthesized under the same conditions exhibited carbonate substitution (Scheverin et al., 2022a). However, in this case, these signals cannot be solely assigned to the presence of carbonates in the structure, as the lignocellulosic matrix presents bands in this zone that are attributable to carbonyl groups ($\text{C}=\text{O}$, RCOOH , RCOOR , etc.) (Morán et al., 2008). Hence it is possible to consider an overlapping contribution of both types of signals to the mentioned bands.

Bands located at 2954, 2922, and 2852 cm^{-1} can be attributed to C–H stretching modes from biomass surface groups. However, the typical biomass signals in 1200–1000 cm^{-1} range (C–O, C=C, etc.) are not detected in the spectrum of HAp–CM. This absence could be explained by the intensity of the $\nu_3 \text{PO}_4^{3-}$ band. On the other hand, in a previous study, we confirmed that the interaction between hydroxyapatite and biomass originates from the interaction with the carbonyl groups present in the lignocellulosic matrix (Scheverin et al., 2022a).

Materials containing hydroxyapatite exhibit a distinct signal at 3500 cm^{-1} associated with the structural OH groups of the mineral. This signal is not observed in the HAp–CM spectrum. However, it is present in the FTIR spectra of HAp (hydroxyapatite) and HAp–C (hydroxyapatite–biomass nanocomposite) constituent materials synthesized under the same conditions (Scheverin et al., 2022a). The absence of this signal in the HAp–CM spectrum suggests the involvement of O–H structural bonds of the mineral in the FeO–HAp interaction (Scheverin et al., 2022b).

On the other hand, the characteristic signal associated to iron oxides ($\nu \text{Fe–O}$), typically found within the 600–500 cm^{-1} range, is not observed in the spectrum. This fact can be explained by considering the high-intensity nature of the $\nu_4 \text{O–P–O}$ bands, causing complete overlap with the Fe–O band in this spectral region. Additionally, it should be considered that the proportion in which iron oxide is present is considerably lower than the proportion of hydroxyapatite in the nanocomposite at least nominally. In this sense, similar results have been reported by other authors working on materials synthesized in a ratio similar to

that used in this work (Bhatt et al., 2020; Scheverin et al., 2022b).

Also, both shape and intensity ratio of bands linked to the $\nu_3 \text{P–O}$ and $\nu_4 \text{O–P–O}$ vibrational modes exhibit marked changes in the magnetic nanocomposite compared to its predecessor materials. Table 2 provides a comparison of the ν_3/ν_4 area ratio of all materials. The results show a notable decrease in the ν_3/ν_4 ratio in the magnetic composite, while this ratio remains constant in the spectra of its HAp and HAp–C precursors. These results indicate significant changes in the chemical environment of the P–O and O–P–O bonds attributed to the presence of iron oxide in the nanocomposite, thereby confirming the presence of iron oxides in the composite.

X-ray diffraction (XRD)

Figure 3 shows the XRD diffractogram pattern of the magnetic nanocomposite. The following diffraction peaks were observed at $2\Theta=25.86, 28.10, 28.70, 31.80, 32.10, 39.84,$ and 46.74 matching well with the (h k l) planes of (0 0 2), (1 0 2), (2 1 0), (2 1 1), (1 1 2), (1 3 0), and (2 2 2), respectively. These peaks are attributed to the hexagonal phased hydroxyapatite in the p63/m space group (ICDD 00-024-0033). The results reveal that no notable changes occurred in the positions of the relevant reflections concerning the standard patterns. Therefore, the composite retains the crystalline structure of hydroxyapatite.

The presence of iron oxides is also verified by the typical signals ascribed to their crystalline pattern. It is important to highlight that magnetite and maghemite cannot be distinguished by XRD because they share the same spinel structure and almost identical lattice parameters (Darminto et al., 2011; Kim

Table 2 Comparison of $\nu_3 \text{P–O} / \nu_4 \text{O–P–O}$ area ratio for hydroxyapatite-based materials synthesized under the same conditions

| Material | $\nu_3 \text{P–O} / \nu_4 \text{O–P–O}$ |
|--------------------|---|
| HAp ^a | 3.94 |
| HAp–C ^b | 3.96 |
| HAp–CM (this work) | 3.39 |

^aHAp=hydroxyapatite

^bHAp–C=hydroxyapatite–biomass composite

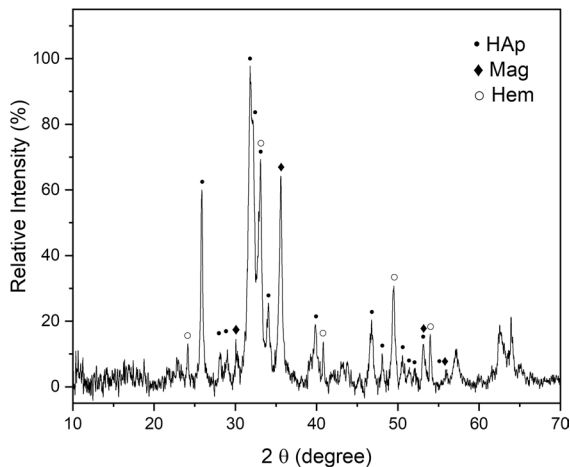


Fig. 3 XRD pattern of HAp-CM in the 2θ range from 10° to 70°

et al., 2012). The position and intensity of peaks at $2\theta = 30.19$, 35.60 , and 56.94 shows a good match with the (h k l) plane of (2 2 0), (3 1 1), and (5 1 1), respectively, of cubic structure magnetite (ICDD 00-019-0629) or eventually maghemite (ICDD 00-039-1346) patterns. On the other hand, the peak at 24.16 confirms the presence of hematite (Hem). The presence of impurities can be ascribed to the synthesis conditions as it was not carried out under inert atmospheric conditions, leading to the partial oxidation of Fe^{2+} ions to Fe^{3+} . This hindered the possibility of exclusively forming magnetite/maghemite (Maity & Agrawal, 2007). Thus, the effective $\text{Fe}^{3+}/\text{Fe}^{2+}$ ratio

increases concerning the initial nominal ratio of 2:1, causing the formation of oxides iron compounds.

The sizes of the magnetite and hydroxyapatite crystallites in the nanocomposite were determined from the Scherrer formula. The size of the magnetite crystallite was 33.3 nm, while that of hydroxyapatite was 13.5 nm. The value obtained for hydroxyapatite crystallite was considerably lower than that obtained for HAp (27.6 nm) and HAp-C (20.6 nm) synthesized under the same conditions and reported in a previous work (Scheverin et al., 2022a). This result suggests that the presence of magnetite hindered the growth of hydroxyapatite onto the nanocomposite.

Electronic microscopic analysis

The surface morphology of HAp-CM was analyzed using TEM and SEM-EDS. The TEM micrograph (Fig. 4) shows particles ranging in size from 10 to 100 nm dispersed throughout the biomass matrix, forming some agglomerated regions, in the typical structure of hybrid organic-inorganic nanocomposite (Horst et al., 2015; Lassalle et al., 2011). In particular, the rod-like particles are due to the hydroxyapatite phase present in the nanocomposite (Mohd Pu'ad et al., 2019; Scheverin et al., 2022a). Additionally, different iron oxide phases in the magnetic nanocomposite can be observed. Particles with an irregular cubic morphology are associated with magnetite/maghemite nanoparticles (Torres-Gómez et al., 2019), while those with a needle-like shape can be

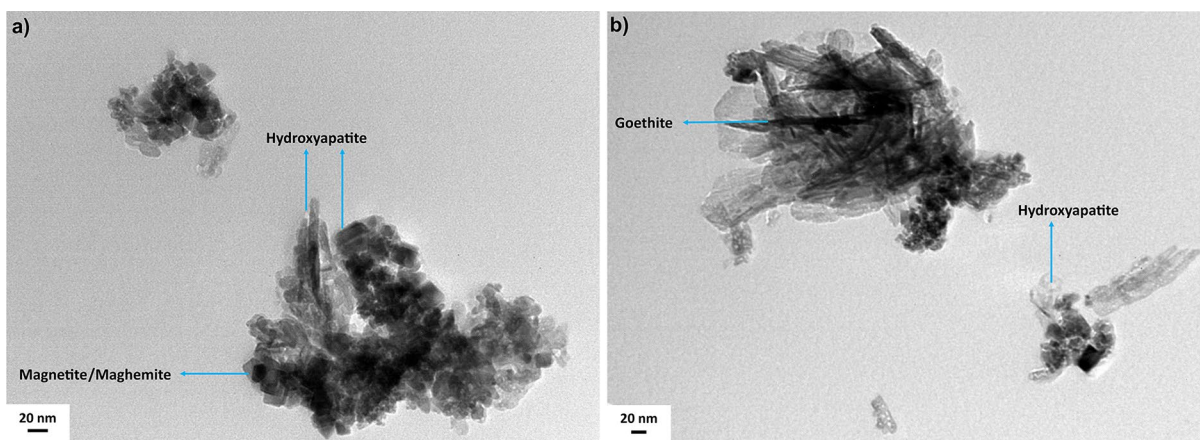


Fig. 4 TEM micrograph of HAp-CM at **a** 270 k x and **b** 200 k x

linked to hematite or goethite (Glotch & Kraft, 2008; Mohammed et al., 2017).

The SEM micrographs show the formation of irregular and porous surface clusters (Fig. S1). Compared to its non-magnetic predecessor (HAp-C), the surface of the magnetic nanocomposite is qualitatively more porous. This observation would indicate that magnetite is deposited on the surface of HAp-C. However, the iron oxide phase cannot be distinguished from the hydroxyapatite phase.

Further, the EDS analysis was performed to determine the elemental composition of the synthesized nanocomposite in terms of iron (Fe), oxygen (O), calcium (Ca), phosphorus (P), and sodium (Na) in a semiquantitative way, considering the limitations of this technique concerning the homogeneity of the analyzed sample. The results obtained from the average of three spectra along with the associated standard deviation are summarized in Table 3. The presence of Na arises from the synthesis conditions since NaOH was used as a precipitating agent. Na⁺ ions can be incorporated into the hydroxyapatite network replacing Ca²⁺ ions, which, in turn, generates a charge balance that favors the substitution of some PO₄³⁻ groups by CO₃²⁻ (B-site carbonate substitution) (Kovaleva et al., 2009).

The Ca/P molar ratio is estimated to be 1.78, which would exceed the expected Ca/P molar ratio for stoichiometric hydroxyapatite (1.67). This difference would indicate that the hydroxyapatite phase obtained would not be stoichiometric. The higher Ca/P ratio could be due to B-site carbonate substitution, aligning with the FTIR findings.

The Fe data further confirms the incorporation of magnetite into the hydroxyapatite-biomass composite. The Ca/Fe molar ratio estimated by SEM-EDS is about 1.30, significantly lower than the nominal Ca/Fe molar theoretical ratio (3.07). This marked

difference could be explained by the fact that the iron oxides are not uniformly distributed throughout the volume but rather deposited on the hydroxyapatite surface, coating it. On the other hand, the element mapping (Fig. S2) reveals a mostly uniform surface distribution of elements composing HAp-CM. Thus, SEM-EDS, FTIR, and XRD characterizations confirm the successful formation of the nanocomposite through the proposed method. However, it's crucial to consider that SEM-EDS characterization might lack representativeness, focusing on a limited area that could not fully reflect the overall sample composition. This is even more critical when non uniform samples are analyzed.

Point of zero charge measurements (pH_{pzc})

Measurement of pH_{pzc} provides information on surface changes related to the total net charge. At pH_{pzc}, both the positive and negative charges developed on the material's surface are in total equilibrium, leaving the net charge equal to zero. When pH levels are below the pH_{pzc}, the surface of the material develops a positive charge due to protonation of its functional groups. Conversely, when pH levels surpass the pH_{pzc}, the adsorbent surface becomes negatively charged because of the deprotonation of surface groups. Therefore, determining the pH_{pzc} is crucial for understanding potential adsorption mechanisms of pH-sensitive adsorbents.

Figure 5 shows the curve of ΔpH versus initial pH obtained using the drift method. The value of pH_{pzc} for HAp-CM was 6.90. At this point, it is important to remark that pH_{pzc} found for its non-magnetic predecessor, HAp-C, was 7.41. The difference between the recorded values is considered additional evidence of the deposition of magnetite on HAp-C's surface, forming a distinct compound with specific properties.

As observed in previous work (Scheverin et al., 2022a), for initial pH values between 6 and 9, the pH_f is nearly equal to the pH_{pzc} value (±0.4). Thus, the magnetic adsorbent acts like a buffer in the studied pH range, revealing its amphoteric behavior.

It should be noted that it was not possible to determine the pH value of the isoelectric point of the material by Z-potential measurements since the system continuously evolves towards the same final pH value (7.0±0.5) regardless of the initial pH value. In this

Table 3 Elemental composition of HAp-CM by SEM-EDS

| Element | Weight (%) |
|---------|--------------|
| Ca | 18.67 (9.82) |
| P | 7.82 (3.8) |
| Fe | 20.03 (7.77) |
| O | 50.10 (8.7) |
| Na | 2.08 (2.31) |

Note: values in parentheses indicate standard deviation

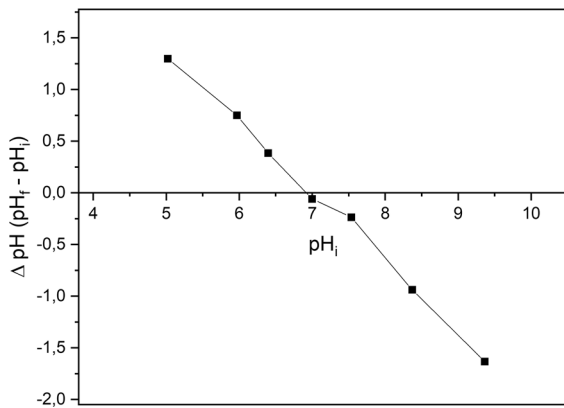


Fig. 5 Graph of ΔpH versus initial pH obtained using the pH drift method

sense, the average zeta potential value registered was -19.20 ± 0.80 mV for this range of final pH values.

Adsorption assays

In general terms, it is known that several factors affect the adsorption process, such as contact time, the pollutant's initial concentration, the amount of adsorbent, and pH, among others. These factors must be optimized to obtain the maximum adsorption capacity. In the following section, we discuss, firstly, the effect of the parameters mentioned above on the adsorption of As and F^- in mono-component systems. Then, we analyze the effect of the presence of different co-ions in an aqueous matrix on adsorption capacity and the competitive adsorption between As and F^- . Finally, we explore the efficiency of the materials as adsorbents using a natural water sample.

Effect of contact time and kinetic modelling

Figure 6 shows the effect of contact time on the adsorption capacity (Q) of HAp-CM. Both pollutants, As and F^- , presents a similar adsorption trend. However, the adsorption of As on the magnetic nanocomposite rapidly reaches equilibrium at 60 min. Meanwhile, F^- adsorption shows a slower increase compared to arsenic, reaching equilibrium after 120 min. As a result, 60 min and 150 min were deemed optimal contact times for further testing of As and F^- , respectively.

Under the explored conditions, the arsenic adsorption capacity at equilibrium (Q_e) was 3.4 mg As per gram of adsorbent, resulting in a 34% removal of the metalloid. Similarly, Q_e for fluoride removal was 3.0 mg $F^- g^{-1}$, representing a 50% removal efficiency. However, the Q_e recorded for fluoride adsorption is lower than that registered for its precursor, HAp-C (4.1 mg F^- per gram of adsorbent), under identical experimental conditions. One possible explanation for these results is that neither magnetite nor biomass showed a quantifiable removal capacity for F^- under the explored conditions. Consequently, the F^- removal capacity of HAp-CM is mainly attributed to the hydroxyapatite phase. Therefore, it is logical that the F^- adsorption capacity (Q_e) to be lower in HAp-CM, as the proportion of hydroxyapatite per gram of material is lower in Hap-CM compared to the hydroxyapatite-biomass nanocomposite.

The experimental data were fitted by non-linear regression analysis to PFO, PSO, and the Weber-Morris model to obtain information regarding adsorption kinetic and potential interaction mechanisms involved in the adsorption process. Table 4 shows the fitting results of the kinetic models for both contaminants.

Arsenic's kinetic data are well described by both PFO and PSO models. However, the difference between the experimental and calculated Q_e is less for the PSO kinetic model than for the PFO model. Furthermore, the statistical parameters χ^2 and R^2 indicate that the PSO model is the one that best fits the experimental data.

For fluoride adsorption, the statistical analysis shows that the PSO model is more appropriate than the PFO to explain the kinetic behavior. Accordingly, the predicted Q_e is very close to the experimental value (3.0 mg $F^- g^{-1}$). Moreover, comparing the kinetic PSO model parameters values for K_2 and h for both contaminants, it is evident that the adsorption process of arsenic onto HAp-CM is faster than the fluoride adsorption.

The adsorption mechanism is a multi-stage process involving bulk diffusion, external diffusion, intraparticle diffusion, and attachment via physisorption or chemisorption (Lima et al., 2015; Tran et al., 2017). In this respect, the Weber-Morris model can estimate the mechanisms involved in the adsorption process and predict the rate-controlling step (Lima et al., 2015).

Fig. 6 Effect of contact time in the **a** arsenic and **b** fluoride adsorption on HAp-CM. The error bars represent the standard deviation of samples. C_{iAs} : 10 mg L^{-1} , C_{iF} : 6 mg L^{-1} , adsorbent dose: 1 g L^{-1} , pH 6, 298 K

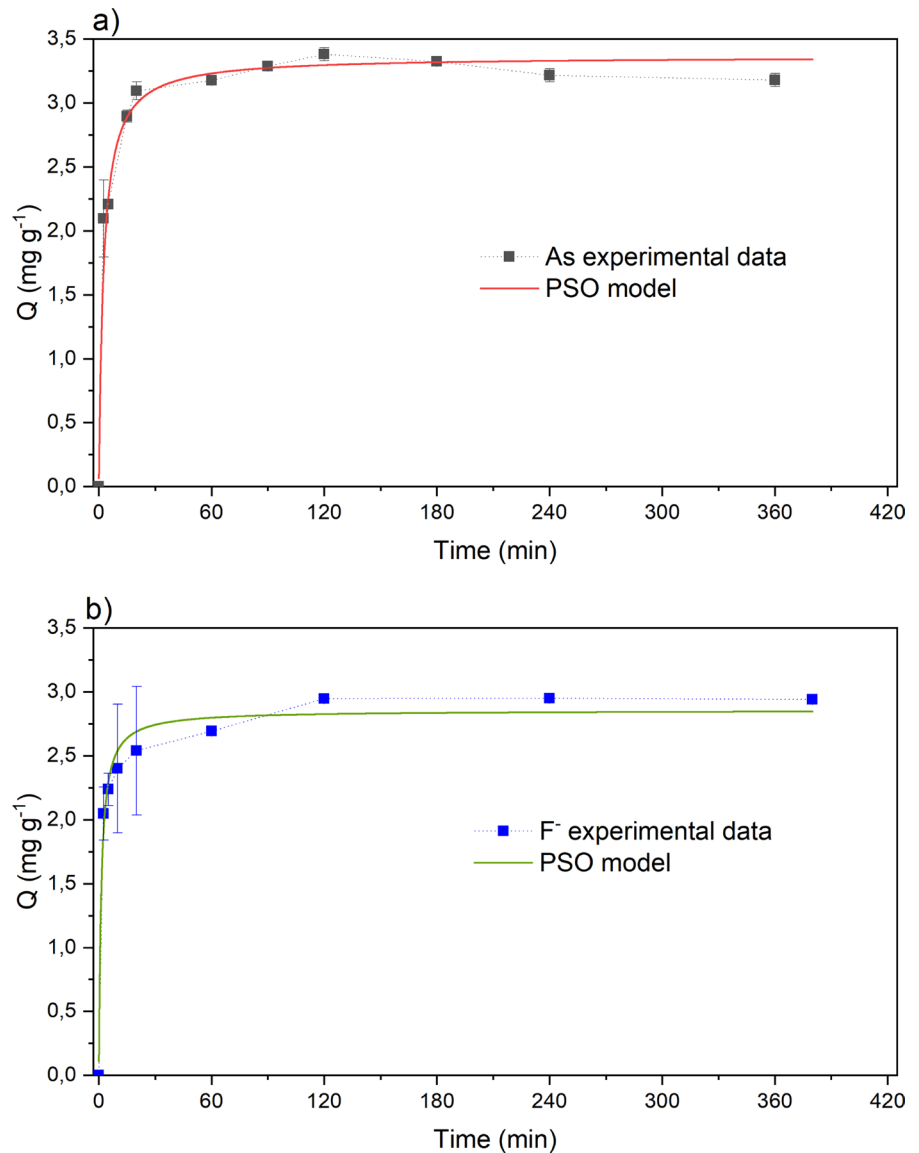


Table 4 Kinetic parameters for arsenic and fluoride adsorption

| Model | R ² | χ ² | Q _e model | Q _e exp | Kinetic parameters |
|----------|----------------|----------------|-------------------------|------------------------|---|
| Arsenic | | | | | |
| PFO | 0.97 | 0.03 | 3.23 mg g ⁻¹ | 3.4 mg g ⁻¹ | K ₁ =0.21 min ⁻¹ |
| PSO | 0.99 | 0.01 | 3.36 mg g ⁻¹ | 3.4 mg g ⁻¹ | K ₂ =0.12 g (mg min) ⁻¹ |
| Fluoride | | | | | |
| PFO | 0.59 | 0.14 | 2.73 mg g ⁻¹ | 3.0 mg g ⁻¹ | K ₁ =0.45 min ⁻¹ |
| PSO | 0.87 | 0.04 | 2.85 mg g ⁻¹ | 3.0 mg g ⁻¹ | K ₂ =0.28 g (mg min) ⁻¹ |

Figure S3 presents the kinetic data for As and F⁻ plotted using the Weber-Morris model. Both resulting plots exhibit multilinearity, indicating that

intraparticle diffusion is not the only rate-limiting step for the sorption process. While the external diffusion stage is not observed, it can be assumed

to have occurred rapidly within the initial few minutes of testing (as shown by the dotted line). The intraparticle diffusion stage can be attributable to the graphs' first linear section (solid line); while the second linear section (dashed line) may depict the equilibrium phase. These results suggest the complexity of the mechanisms involved in the adsorption of As and F^- onto the magnetic hydroxyapatite–biomass nanocomposite. They indicate that intra-particle diffusion isn't the sole factor governing the adsorption of both contaminants.

On the other hand, the slope of the first linear portion allows obtaining the intraparticle diffusion rate. As shown in Fig. S3 (supplementary material), the intraparticle rate for As ($K_{id}=0.408 \text{ mg (g} \times \text{min)}^{-1/2}$) is about five times higher than that presented for F^- adsorption ($K_{id}=0.08 \text{ mg$

$(\text{g} \times \text{min)}^{-1/2}$). These results are consistent with the conclusions derived from the PSO model study.

Effect of initial concentration and isotherm modeling

The study of the effect of initial concentration and isotherm modeling describes how an adsorbate interacts with the adsorbent under equilibrium conditions. Notably, isotherm modeling provides valuable information about maximum adsorption capacity (Q_{\max}) and the possible mechanism involved in the adsorption process, facilitating comparisons among different materials.

Langmuir and Freundlich's models were applied to elucidate the behavior observed in the experimental data. Figure 7 and Table 5 show the fit of the two models and the statistical parameters. Either model can successfully explain the As or F^- adsorption onto

Fig. 7 Adsorption isotherm for **a** Arsenic and **b** Fluoride adsorption on HAp–CM—The error bars represent the standard deviation of samples. Adsorbent dose: 1 g L^{-1} , pH 6, 60 min, 298 K

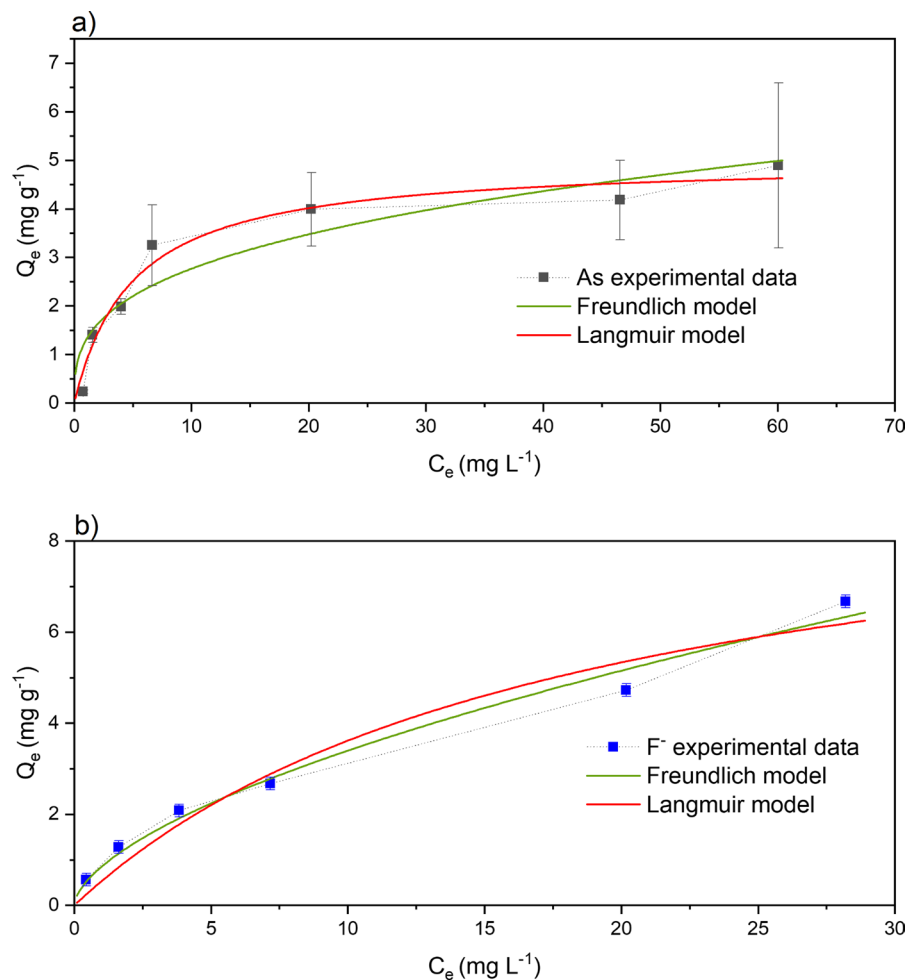


Table 5 Characteristic parameters of different isotherm modeling for arsenic and fluoride adsorption

| Model | Arsenic | | | Fluoride | | |
|---------------------|----------------|----------------|--|----------------|----------------|--|
| | R ² | χ ² | Isotherm constants | R ² | χ ² | Isotherm constants |
| Langmuir isotherm | 0.991 | 0.44 | Q _{max} = 5.00 mg g ⁻¹ K _L = 0.20 L mg ⁻¹ | 0.987 | 0.85 | Q _{max} = 10.20 mg g ⁻¹ K _L = 0.06 L mg ⁻¹ |
| Freundlich isotherm | 0.972 | 1.17 | K _F = 1.30 mg g ⁻¹ (mg L ⁻¹) ^{-1/n} n = 3.04 | 0.995 | 0.10 | K _F = 0.85 mg g ⁻¹ (mg L ⁻¹) ^{-1/n} n = 1.66 |

HAp-CM since the non-linear correlation coefficient is R² > 0.9.

Although both models satisfactorily explain the experimental data, the Langmuir model (χ² = 0.44) provides a better fit for arsenic adsorption compared to the Freundlich model (χ² = 1.7). The high correlation with the Langmuir isotherm suggests that primarily adsorbs onto the adsorbent’s surface in a monolayer coverage manner. Conversely, the Freundlich model (χ² = 0.10) better fits the fluoride adsorption than the Langmuir model (χ² = 0.85), indicating that F⁻ predominantly adheres to the adsorbent’s surface in a heterogeneous manner.

HAp-CM exhibits a Q_{max} of 5.0 and 10.2 mg g⁻¹ for As and F⁻ removal, respectively. The fluoride Q_{max} of HAp-CM (10.2 mg L⁻¹) is almost equal to the Q_{max} value presented by its non-magnetic predecessor material, HAp-C (10.0 mg L⁻¹). On the other hand, K_F values demonstrate that HAp-CM has a major affinity for As (1.30) than F⁻ (0.85).

Effect of the adsorbent dose

To investigate the effect of the adsorbent dose, a series of adsorption experiments were conducted using varying amounts of HAp-CM, ranging from 1 to 4 g L⁻¹, while maintaining initial concentrations of 10 mg L⁻¹ for As and 6 mg L⁻¹ for F⁻. Table S1 shows the influence of the adsorbent dosage on As and F⁻ removal. As shown, there’s a substantial increase in removal percentage as the HAp-CM dosage rises, which implies that Q decreases for both contaminants.

The efficiency of fluoride adsorption increases from 48.2 to 86.07% with an increment of the adsorbent amount from 1 to 4 g L⁻¹, resulting in a decrease in F⁻ concentration in the aqueous solution from 6.00 to 0.84 mg L⁻¹, the WHO’s maximum limit of 1.5 mg L⁻¹. Likewise, arsenic removal efficiency increased

from 30.1 to 76.1% with the same rise in adsorbent quantity. Despite achieving high removal percentages for As, the final concentration values exceeded the recommended maximum limit of 0.01 mg L⁻¹. Notably, the initial As concentrations were unusually high, far beyond typical levels found in groundwater sources (Kumar et al., 2020). Consequently, we decided not to explore higher adsorbent dosages.

Effect of pH

The influence of pH is an important factor to evaluate since both the structure and charge of the adsorbent and adsorbate can change with variations in pH. This is particularly important because real water samples vary widely in pH due to their diverse sources. Consequently, the adsorption efficiency could fluctuate concerning pH value, depending on the sorption process mechanism. Figure 8 shows the effect of the initial pH HAp-CM’s efficiency for As and F⁻ removal.

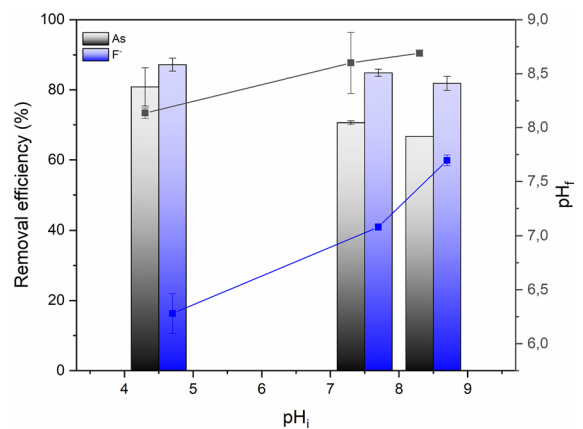


Fig. 8 Effect of pH on the on the arsenic and fluoride removal capacity. The error bars represent the standard deviation of samples

The extent of As adsorption peaks at pH 4.5 (80.86%) and declines as pH increases. This trend is attributed to pH's influence on both arsenic speciation and the adsorbent's surface charge. As pH rises, it prompts the successive deprotonation of arsenic species, altering their affinity for the adsorbent. Simultaneously, the surface charge on HAp-CM is also influenced by pH's solution. As detailed in Sect. "Point of zero charge measurements (pH_{pzc})", HAp-CM's surface is negatively charged beyond the pH_{pzc} (7.41). Then, at pH > pH_{pzc}, electrostatic repulsion between arsenic species and HAp-CM nanoparticles diminishes adsorption efficiency. Thus, these results show that the arsenic mechanism adsorption involves a strong contribution of electrostatic forces.

The efficiency of F⁻ adsorption moderately decreases (<6%) with increasing pH. Therefore, the fluoride adsorption process of HAp-CM is not strongly pH-dependent. Thus, the electrostatic forces are not the predominant mechanism for fluoride adsorption.

Analysis of final solution pH values post-fluoride adsorption reveals that ΔpH > 0 when the initial solution pH was lower than pH_{pzc}. Conversely, ΔpH < 0 occurs when the initial pH exceeds pH_{pzc}. A similar trend was found using its non-magnetic predecessor (HAp-C) and by other authors using hydroxyapatite (Jiménez-Reyes & Solache-Ríos, 2010; Medellín-Castillo et al., 2014; Poinern et al., 2011), and iron oxide-based materials (Deng & Yu, 2012). In this context, fluoride adsorption occurs through ligand exchange with OH⁻ surface groups, causing a pH increase. However, it's reported that at basic pH values, the OH⁻ content in the solution competes with F⁻ ions for sorption sites in the sorbent material, resulting in ΔpH < 0 (Gómez Hortigüela et al., 2014; Jiménez-Reyes & Solache-Ríos, 2010; Sundaram et al., 2008).

Effect of coexisting ions

The removal of As and F⁻ from groundwater sources may be hampered due to coexisting species competing for the active sites on the adsorbent. Chlorides (Cl⁻), nitrate (NO₃⁻), bicarbonate (HCO₃⁻), sulfate (SO₄²⁻), phosphate (PO₄³⁻), sodium (Na⁺), and calcium (Ca²⁺) are among the species commonly found in high concentrations in groundwater (Ravindra & Garg, 2007; Tatawat & Chandel, 2008). These various species

could potentially have either a positive or negative impact on pollutant removal. To understand the influence of coexisting ions on As and F⁻ removal efficiency, solutions of each pollutant were spiked with Cl⁻, HCO₃⁻, NO₃⁻, SO₄²⁻, PO₄³⁻, and Ca²⁺ (250 mg L⁻¹). Then, the percentage of As or F⁻ removal was calculated. It's noteworthy that in these experiments, we adjusted the pH value to 8.5 to replicate natural water sample conditions. Figure 9 depicts the effect of coexisting ions on arsenic and fluoride removal efficiency (% R) on HAp-CM.

Most co-ions studied enhance the efficiency of arsenic adsorption, except for PO₄³⁻. Interestingly, the presence of PO₄³⁻ greatly inhibited arsenic adsorption, reducing the efficiency from 66 to 9%. This inhibition could be attributed to the structural and chemical similarities between PO₄³⁻ ions and arsenic species (Lin et al., 2012). Studies have indicated that both are adsorbed as inner-sphere complexes onto iron oxides (Arai & Sparks, 2001; Gallegos-Garcia et al., 2012). On the contrary, arsenic uptake increases by about 29% in the presence of Ca²⁺. In this regard, it is widely reported that Ca²⁺ ions positively impact arsenic removal enhancing electrostatic attraction and the co-precipitation process (Mohan & Pittman, 2007).

The presence of Cl⁻, HCO₃⁻, SO₄²⁻, and NO₃⁻ notably has a positive impact, resulting in an increase of nearly 32% in removal efficiency,

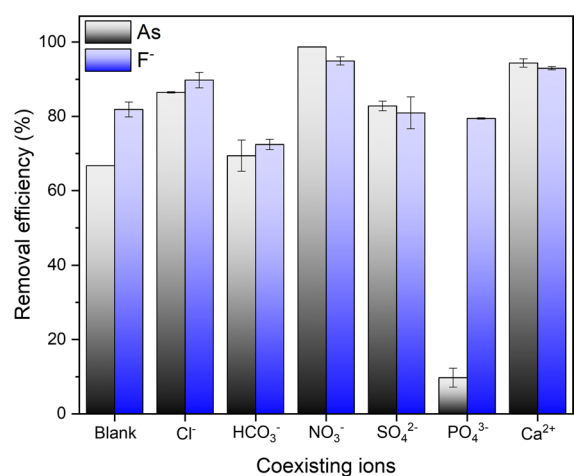


Fig. 9 Effect of the presence of coexisting ions on the As and F⁻ removal efficiency of HAp-CM. The error bars represent the standard deviation of samples

particularly when NO_3^- ions are present. It's important to note that while these mentioned anions typically decrease arsenic uptake, especially NO_3^- ions (Mohan & Pittman, 2007), this effect is not the case for As adsorption on HAp-CM. Further characterizations beyond the scope of this work are required to explain the abovementioned phenomenon. These results demonstrate some of the advantages that could be generated by the synthesis of this type of composite material for application in groundwater treatment.

The adsorption of fluoride has different behavior depending on the coexisting species. The presence of Cl^- , NO_3^- y Ca^{2+} improves the efficiency of F^- removal. Meanwhile, the presence of coexisting anions such as PO_4^{3-} , SO_4^{2-} y HCO_3^- result in a reduction of F^- adsorption efficiency. Overall, the differences in the percentage removal (Δ %) observed for F^- adsorption are notably smaller than those recorded for As. Then, the efficiency of F^- removal is less influenced by the presence of coexisting species compared to As removal.

Competitive adsorption

The coexistence of arsenic and fluorides in groundwater typically shows a positive correlation. For this reason, the competitive adsorption between As and F^- on HAp-CM was studied. The experiments were performed with an initial concentration of 6 mg L^{-1} F^- with two distinct arsenic concentrations: 10 mg L^{-1} As and 0.250 mg L^{-1} As. It's worth noting that the selection of low arsenic concentration levels and the fixed F^- concentration was based on previous reports detailing contaminant levels in the groundwater of Buenos Aires Province, Argentina (Argentina) (Al Rawahi, 2016).

Table 6 provides the equilibrium data and adsorption yield. The results demonstrate synergistic behavior in fluoride adsorption when high arsenic concentrations are present, showing an increase in removal efficiency from 81.8% to 93.5%. Additionally, fluoride removal sees a slight 2% increase as arsenic concentration decreases from 10 mg L^{-1} to 0.250 mg L^{-1} .

On the other hand, with an initial arsenic concentration of 10 mg L^{-1} , As removal also demonstrates synergistic behavior, with the removal percentage escalating from 66.7% to 88.7% in the presence of fluoride. For low arsenic concentrations, neither the

Table 6 Parameters of competitive adsorption between As and F^- on HAp-CM

| | As $C_i = 10 \text{ mg L}^{-1}$ | | As $C_i = 0.250 \text{ mg L}^{-1}$ | |
|------------------------------|---------------------------------|--------------|------------------------------------|--------------|
| | As | F^- | As | F^- |
| C_F (mg L^{-1}) | 1.17 (0.02) | 0.39 (0.04) | <0.01 | 0.29 (0.01) |
| Q mg g^{-1} | 2.20 (0.002) | 1.40 (0.01) | >0.01 | 0.09 (0.03) |
| R (%) | 88.7 (0.22) | 93.5 (0.68) | >96.0 | 95.1 (0.21) |

Note: values in parentheses indicate standard deviation

adsorption capacity nor the removal efficiency could be calculated due to the final As concentration falling below the quantification limit of the method used (Sect. "Batch adsorption assays"). Nevertheless, it's evident that even at low concentrations, the arsenic removal capacity is sufficiently high to reduce the levels below the established WHO limit.

Natural water assessments

The efficiency of the HAp-CM nanocomposite in treating naturally contaminated groundwater containing As and F^- was evaluated. As depicted in Table 1, the initial fluoride concentration in the water sample was 3.06 mg L^{-1} , which greatly exceeded the WHO guideline range of $0.5\text{--}1.5 \text{ mg L}^{-1}$. Moreover, the arsenic concentration was 0.116 mg L^{-1} , surpassing the recommended limit of 0.01 mg L^{-1} .

Figure 10 presents the results of testing the HAp-CM's efficiency in removing As and F^- over five consecutive adsorption cycles. The data indicates that within the first four cycles, F^- concentrations were effectively reduced below the maximum recommended limit. However, the percentage of F^- removal gradually declined in subsequent cycles.

In the first cycle of As removal, the removal percentage surpassed 91% reducing the concentration to a permissible level of 0.01 mg L^{-1} . Despite consistently high removal percentages in subsequent cycles, achieving the recommended limits for arsenic concentration were not possible. These results can be explained by considering the presence of multiple species in the sample that can compete for active sites of the adsorbent.

It is worth noting that employing adsorbents effectively in natural environments such as groundwater requires a tailored approach. This involves evaluating

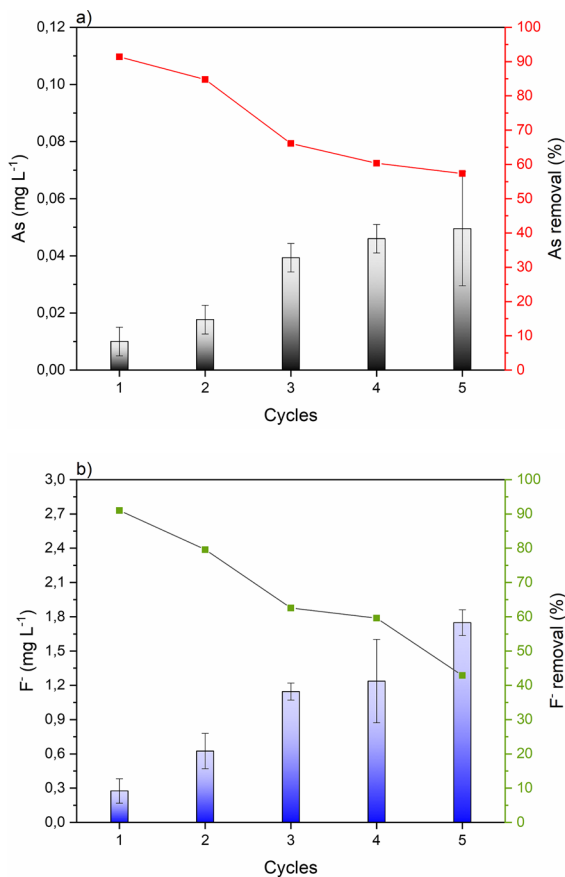


Fig. 10 Cycles of reuse of HAp-CM for **a** As and **b** F⁻ adsorption in a groundwater sample

specific factors like the ratio of adsorbent mass to volume or pre-treating water to eliminate potential interfering species (Burriss and Juenger, 2016). These considerations help optimize the adsorption conditions and ensure efficient removal of contaminants from the water source under study.

Monitoring the stability of materials Stability is a crucial property to consider when evaluating the feasibility of the using adsorbent materials. The undesired

leaching of these materials' components into treated water necessitates careful evaluation. To assess this property in groundwater treatment, the amount of iron and calcium over five consecutive reuse cycles was evaluated as parameters of HAp and iron oxides components of nanocomposites. Table 7 shows the results of this evaluation.

The data indicates the stability of HAp-CM concerning both selected elements. Notably, there was no detection of calcium leaching throughout the reuse cycles. Conversely, concerning iron, not only was there no leaching observed into the medium, but continuous metal adsorption was recorded consistently across all consecutive reuse cycles. These results highlight HAp-CM's capability to retain iron within its structure, establishing it as a promising adsorbent for water treatment applications.

Conclusions

In this research, a novel magnetic hydroxyapatite-bio-mass nanocomposite (HAp-CM) was successfully synthesized using a combined sonochemical/hydrothermal approach to removing arsenic and fluoride from groundwater. This material demonstrated to exhibit suitable physicochemical properties regarding its potential for groundwater remediation.

Comprehensive characterization techniques were employed to confirm the structure and composition of HAp-CM. The nanocomposite showed noteworthy adsorption capacities for both contaminants, following pseudo-second-order kinetics, with equilibrium times of 60 min for arsenic and 150 min for fluoride. Its maximum adsorption capacity was 5.0 mg g⁻¹ for As and 10.2 mg g⁻¹ for F⁻. pH levels notably influenced the adsorption capacity for both pollutants under study. Coexisting ions had distinct impacts on fluoride removal and increased arsenic adsorption, except for PO₄³⁻. Moreover, a synergistic effect was observed when both contaminants were present.

Table 7 HAp-CM stability in groundwater in terms of Ca and Fe

| | Initial | Cycle 1 | Cycle 2 | Cycle 3 | Cycle 4 | Cycle 5 |
|--------------------------|--------------|----------------|----------------|----------------|---------------|----------------|
| Ca (mg L ⁻¹) | 70.70 (0.77) | 65.60 (0.94) | 66.00 (4.54) | 70.22 (0.78) | 71.33 (0.67) | 72.22 (1.02) |
| Fe (mg L ⁻¹) | 0.14 (0.001) | 0.038 (0.0038) | 0.0041 (0.001) | 0.0485 (0.005) | 0.048 (0.001) | 0.060 (0.0009) |

Note: values in parentheses indicate standard deviation

Test on naturally contaminated groundwater highlighted HAP–CM's efficiency in reducing fluoride concentrations over multiple cycles, while arsenic removal met recommended levels only initially. Despite this, the adsorbent proved stable in real environmental conditions, underscoring its potential for treating contaminated water sources.

Acknowledgements The authors acknowledge the financial support of UNS (Universidad Nacional del Sur, Argentina; CONICET, Argentina; and ANPCyT, Argentina).

Author contributions V. N. Scheverin: investigation, methodology, formal analysis, visualization, and Writing—original draft. E.M Díaz: methodology and formal analysis. M. F. Horst: conceptualization, supervision, project administration, founding acquisition, resources, and writing—review & editing. V. L. Lassalle: conceptualization, supervision, project administration, founding acquisition, resources, and writing—review & editing.

Funding This work was supported by the National Council of Scientific and Technological Research (CONICET) and the National Agency for the Promotion of Science, Technology and Innovation (ANPCYT), Grant number: PICT 2018 3476; and the National University of South (UNS, Bahía Blanca, Argentina) Grant number 24/Q125.

Declarations

Competing interests The authors declare no competing interests.

References

- Al Rawahi, W. (2016). *Vanadium, arsenic and fluoride in natural waters from Argentina and possible impact on human health*. Guildford: University of Surrey.
- Alarcón-Herrera, M. T., Bundschuh, J., Nath, B., Nicolli, H. B., Gutierrez, M., Reyes-Gomez, V. M., Nuñez, D., Martín-Dominguez, I. R., & Sracek, O. (2013). Co-occurrence of arsenic and fluoride in groundwater of semi-arid regions in Latin America: Genesis, mobility and remediation. *Journal of Hazardous Materials*, 262, 960–969. <https://doi.org/10.1016/j.jhazmat.2012.08.005>
- Arai, Y., & Sparks, D. L. (2001). ATR-FTIR spectroscopic investigation on phosphate adsorption mechanisms at the ferrihydrite-water interface. *Journal of Colloid and Interface Science*, 241(2), 317–326. <https://doi.org/10.1006/jcis.2001.7773>
- Bhatt, A., Sakai, K., Madhyastha, R., Murayama, M., Madhyastha, H., & Rath, S. N. (2020). Biosynthesis and characterization of nano magnetic hydroxyapatite (nMHAp): An accelerated approach using simulated body fluid for biomedical applications. *Ceramics International*, 46(17), 27866–27876. <https://doi.org/10.1016/J.CERAMINT.2020.07.285>
- Biedrzycka, A., Skwarek, E., & Hanna, U. M. (2021). Hydroxyapatite with magnetic core: Synthesis methods, properties, adsorption and medical applications. *Advances in Colloid and Interface Science*, 291, 102401. <https://doi.org/10.1016/J.CIS.2021.102401>
- Burhenne, L., Messmer, J., Aicher, T., & Laborie, M.-P. (2013). The effect of the biomass components lignin, cellulose and hemicellulose on TGA and fixed bed pyrolysis. *Journal of Analytical and Applied Pyrolysis*, 101, 177–184. <https://doi.org/10.1016/j.jaap.2013.01.012>
- Burris, L. E., & Juenger, M. C. G. (2016). The effect of acid treatment on the reactivity of natural zeolites used as supplementary cementitious materials. *Cement and Concrete Research*, 79, 185–193. <https://doi.org/10.1016/j.cemconres.2015.08.007>
- Darminto, Cholishoh, M. N., Perdana, F. A., Baqiya, M. A., Mashuri, Cahyono, Y., & Triwikantoro. (2011). Preparing Fe₃O₄ nanoparticles from Fe²⁺ ions source by co-precipitation process in various pH. *AIP Conference Proceedings*, 1415(2011), 234–237. <https://doi.org/10.1063/1.3667264>
- Deng, H., & Yu, X. (2012). Adsorption of fluoride, arsenate and phosphate in aqueous solution by cerium impregnated fibrous protein. *Chemical Engineering Journal*, 184, 205–212. <https://doi.org/10.1016/j.ccej.2012.01.031>
- Gallegos-García, M., Ramírez-Muñiz, K., & Song, S. (2012). Arsenic removal from water by adsorption using iron oxide minerals as adsorbents: A review. *Mineral Processing and Extractive Metallurgy Review*, 33(5), 301–315. <https://doi.org/10.1080/08827508.2011.584219>
- Glotch, T. D., & Kraft, M. D. (2008). Thermal transformations of akaganéite and lepidocrocite to hematite: Assessment of possible precursors to Martian crystalline hematite. *Physics and Chemistry of Minerals*, 35(10), 569–581. <https://doi.org/10.1007/s00269-008-0249-z>
- Gómez Hortigüela, L., Pérez Pariente, J., & Díaz Carretero, I. (2014). Materiales compuestos de zeolita-hidroxiapatita para la eliminación de fluoruro del agua potable. *Anales De Química*, 110(4), 276–283.
- Habuda-Stanić, M., Ravančić, M., & Flanagan, A. (2014). A review on adsorption of fluoride from aqueous solution. *Materials*, 7(9), 6317–6366. <https://doi.org/10.3390/ma7096317>
- Hao, L., Liu, M., Wang, N., & Li, G. (2018). A critical review on arsenic removal from water using iron-based adsorbents. *RSC Advances*, 8(69), 39545–39560. <https://doi.org/10.1039/C8RA08512A>
- Horst, M. F., Lassalle, V., & Ferreira, M. L. (2015). Nano-sized magnetite in low cost materials for remediation of water polluted with toxic metals, azo- and anthraquinonic dyes. *Frontiers of Environmental Science and Engineering*, 9(5), 746–769. <https://doi.org/10.1007/s11783-015-0814-x>
- Jiménez-Reyes, M., & Solache-Ríos, M. (2010). Sorption behavior of fluoride ions from aqueous solutions by hydroxyapatite. *Journal of Hazardous Materials*, 180(1–3), 297–302. <https://doi.org/10.1016/j.jhazmat.2010.04.030>

- Jung, K.-W., Lee, S. Y., Choi, J.-W., & Lee, Y. J. (2019). A facile one-pot hydrothermal synthesis of hydroxyapatite/biochar nanocomposites: Adsorption behavior and mechanisms for the removal of copper(II) from aqueous media. *Chemical Engineering Journal*, 369(January), 529–541. <https://doi.org/10.1016/j.cej.2019.03.102>
- Kermanian, M., Naghibi, M., & Sadighian, S. (2020). One-pot hydrothermal synthesis of a magnetic hydroxyapatite nanocomposite for MR imaging and pH-Sensitive drug delivery applications. *Heliyon*, 6(9), e04928. <https://doi.org/10.1016/j.heliyon.2020.e04928>
- Khatamian, M., Afshar No, N., Hosseini Nami, S., & Fazli-Shokouhi, S. (2023). Synthesis and characterization of zeolite A, Fe₃O₄/zeolite A, and Fe₂O₃/zeolite A nanocomposites and investigation of their arsenic removal performance. *Journal of the Iranian Chemical Society*. <https://doi.org/10.1007/s13738-023-02787-w>
- Kim, W., Suh, C. Y., Cho, S. W., Roh, K. M., Kwon, H., Song, K., & Shon, I. J. (2012). A new method for the identification and quantification of magnetite-maghemite mixture using conventional X-ray diffraction technique. *Talanta*, 94, 348–352. <https://doi.org/10.1016/j.talanta.2012.03.001>
- Kovaleva, E. S., Shabanov, M. P., Putlyaev, V. I., Tretyakov, Y. D., Ivanov, V. K., & Silkin, N. I. (2009). Bioresorbable carbonated hydroxyapatite Ca_{10-x}Na_x(PO₄)_{6-x}(CO₃)_x(OH)₂ powders for bioactive materials preparation. *Central European Journal of Chemistry*, 7(2), 168–174. <https://doi.org/10.2478/s11532-009-0018-y>
- Kumar, M., Das, A., Das, N., Goswami, R., & Singh, U. K. (2016). Co-occurrence perspective of arsenic and fluoride in the groundwater of Diphu, Assam, Northeastern India. *Chemosphere*, 150, 227–238. <https://doi.org/10.1016/J.CHEMOSPHERE.2016.02.019>
- Kumar, M., Goswami, R., Patel, A. K., Srivastava, M., & Das, N. (2020). Scenario, perspectives and mechanism of arsenic and fluoride Co-occurrence in the groundwater: A review. *Chemosphere*, 249, 126126. <https://doi.org/10.1016/j.chemosphere.2020.126126>
- Lassalle, V. L., Zysler, R. D., & Ferreira, M. L. (2011). Novel and facile synthesis of magnetic composites by a modified co-precipitation method. *Materials Chemistry and Physics*, 130(1–2), 624–634. <https://doi.org/10.1016/j.matchemphys.2011.07.035>
- Lima, E. C., Adebayo, M. A., & Machado, F. M. (2015). Kinetic and Equilibrium Models of Adsorption. In *Carbon Nanostructures* (Vol. 0, Issue 9783319188744, pp. 33–69). https://doi.org/10.1007/978-3-319-18875-1_3
- Lin, S., Lu, D., & Liu, Z. (2012). Removal of arsenic contaminants with magnetic γ -Fe₂O₃ nanoparticles. *Chemical Engineering Journal*, 211–212, 46–52. <https://doi.org/10.1016/J.CEJ.2012.09.018>
- Litter, M. I., Morgada, M. E., & Bundschuh, J. (2010). Possible treatments for arsenic removal in Latin American waters for human consumption. *Environmental Pollution*, 158(5), 1105–1118. <https://doi.org/10.1016/j.envpol.2010.01.028>
- Maity, D., & Agrawal, D. C. (2007). Synthesis of iron oxide nanoparticles under oxidizing environment and their stabilization in aqueous and non-aqueous media. *Journal of Magnetism and Magnetic Materials*, 308(1), 46–55. <https://doi.org/10.1016/j.jmmm.2006.05.001>
- Maity, J. P., Vithanage, M., Kumar, M., Ghosh, A., Mohan, D., Ahmad, A., & Bhattacharya, P. (2021). Seven 21st century challenges of arsenic-fluoride contamination and remediation. *Groundwater for Sustainable Development*, 12, 100538. <https://doi.org/10.1016/j.gsd.2020.100538>
- Medellin-Castillo, N. A., Leyva-Ramos, R., Padilla-Ortega, E., Perez, R. O., Flores-Cano, J. V., & Berber-Mendoza, M. S. (2014). Adsorption capacity of bone char for removing fluoride from water solution. Role of hydroxyapatite content, adsorption mechanism and competing anions. *Journal of Industrial and Engineering Chemistry*, 20(6), 4014–4021. <https://doi.org/10.1016/J.JIEC.2013.12.105>
- Mishra, R. K., & Mohanty, K. (2018). Pyrolysis kinetics and thermal behavior of waste sawdust biomass using thermogravimetric analysis. *Bioresource Technology*, 251, 63–74. <https://doi.org/10.1016/J.BIORTECH.2017.12.029>
- Mohammed, R., El-Maghrabi, H. H., Younes, A. A., Farag, A. B., Mikhail, S., & Riad, M. (2017). SDS-goethite adsorbent material preparation, structural characterization and the kinetics of the manganese adsorption. *Journal of Molecular Liquids*, 231, 499–508. <https://doi.org/10.1016/J.MOLLIQ.2017.02.041>
- Mohan, D., & Pittman, C. U. (2007). Arsenic removal from water/wastewater using adsorbents-A critical review. *Journal of Hazardous Materials*, 142(1–2), 1–53. <https://doi.org/10.1016/j.jhazmat.2007.01.006>
- Mohd P'uad, N. A. S., Abdul Haq, R. H., Mohd Noh, H., Abdullah, H. Z., Idris, M. I., & Lee, T. C. (2019). Synthesis method of hydroxyapatite: A review. *Materials Today: Proceedings*, 29, 233–239. <https://doi.org/10.1016/j.matpr.2020.05.536>
- Morán, J. I., Alvarez, V. A., Cyras, V. P., & Vázquez, A. (2008). Extraction of cellulose and preparation of nanocellulose from sisal fibers. *Cellulose*, 15(1), 149–159. <https://doi.org/10.1007/s10570-007-9145-9>
- Murphy, J., & Riley, J. P. (1962). A modified single solution method for the determination of phosphate in natural waters. *Analytica Chimica Acta*, 27(C), 31–36. [https://doi.org/10.1016/S0003-2670\(00\)88444-5](https://doi.org/10.1016/S0003-2670(00)88444-5)
- Newcombe, G., Hayes, R., & Drikas, M. (1993). Granular activated carbon: Importance of surface properties in the adsorption of naturally occurring organics. *Colloids and Surfaces a: Physicochemical and Engineering Aspects*, 78(C), 65–71. [https://doi.org/10.1016/0927-7757\(93\)80311-2](https://doi.org/10.1016/0927-7757(93)80311-2)
- Nicolli, H. B., Bundschuh, J., Blanco, C., Tujchneider, O. C., Panarello, H. O., Dapeña, C., & Rusansky, J. E. (2012). Arsenic and associated trace-elements in groundwater from the Chaco-Pampean plain, Argentina: Results from 100 years of research. *Science of the Total Environment*, 429, 36–56. <https://doi.org/10.1016/j.scitotenv.2012.04.048>
- Pai, S., Kini, S. M., Selvaraj, R., & Pugazhendhi, A. (2020). A review on the synthesis of hydroxyapatite, its composites and adsorptive removal of pollutants from wastewater. *Journal of Water Process Engineering*, 38, 101574. <https://doi.org/10.1016/j.jwpe.2020.101574>
- Panchu, S. E., Sekar, S., Rajaram, V., Kolanthai, E., Panchu, S. J., Swart, H. C., & Narayana Kalkura, S. (2022). Enriching trace level adsorption affinity of As³⁺ ion using hydrothermally synthesized iron-doped hydroxyapatite

- nanorods. *Journal of Inorganic and Organometallic Polymers and Materials*, 32(1), 47–62. <https://doi.org/10.1007/s10904-021-02103-0>
- Paoloni, J. D., Fiorentino, C. E., & Sequeira, M. E. (2003). Fluoride contamination of aquifers in the southeast subhumid pampa, Argentina. *Environmental Toxicology*, 18(5), 317–320. <https://doi.org/10.1002/tox.10131>
- Pizarro, C., Rubio, M. A., Escudéy, M., Alborno, M. F., Muñoz, D., Denardin, J., & Fabris, J. D. (2015). Nanomagnetite-zeolite composites in the removal of arsenate from aqueous systems. *Journal of the Brazilian Chemical Society*, 26(9), 1887–1896. <https://doi.org/10.5935/0103-5053.20150166>
- Poinern, G. E. J., Ghosh, M. K., Ng, Y. J., Issa, T. B., Anand, S., & Singh, P. (2011). Defluoridation behavior of nanostructured hydroxyapatite synthesized through an ultrasonic and microwave combined technique. *Journal of Hazardous Materials*, 185(1), 29–37. <https://doi.org/10.1016/j.jhazmat.2010.08.087>
- Ravindra, K., & Garg, V. K. (2007). Hydro-chemical survey of groundwater of Hisar city and assessment of defluoridation methods used in India. *Environmental Monitoring and Assessment*, 132, 33–43. <https://doi.org/10.1007/s10661-006-9500-6>
- Rehman, I., & Bonfield, W. (1997). Characterization of hydroxyapatite and carbonated apatite by photo acoustic FTIR spectroscopy. *Journal of Materials Science: Materials in Medicine*, 8(1), 1–4. <https://doi.org/10.1023/A:1018570213546>
- Rocha Amador, D. O. (2005). *Efectos sobre el sistema nervioso central por la exposición simultánea a flúor y arsénico* [Universidad Autónoma de San Luis Potosí]. <https://ninive.uaslp.mx/xmlui/bitstream/handle/i/1815/MCA1E/SS00501.pdf?sequence=3>
- Salema, A. A., Ting, R. M. W., & Shang, Y. K. (2019). Pyrolysis of blend (oil palm biomass and sawdust) biomass using TG-MS. *Bioresour Technol*, 274, 439–446. <https://doi.org/10.1016/j.biortech.2018.12.014>
- Scheverin, V. N., Horst, M. F., & Lassalle, V. L. (2022a). Novel hydroxyapatite–biomass nanocomposites for fluoride adsorption. *Results in Engineering*, 16, 100648. <https://doi.org/10.1016/j.rineng.2022.100648>
- Scheverin, V. N., Russo, A., Grünhut, M., Horst, M. F., Jacobo, S., & Lassalle, V. L. (2022b). Novel iron-based nanocomposites for arsenic removal in groundwater: Insights from their synthesis to implementation for real groundwater remediation. *Environmental Earth Sciences*, 81(7), 188. <https://doi.org/10.1007/s12665-022-10286-z>
- Sundaram, C. S., Viswanathan, N., & Meenakshi, S. (2008). Defluoridation chemistry of synthetic hydroxyapatite at nano scale: Equilibrium and kinetic studies. *Journal of Hazardous Materials*, 155(1–2), 206–215. <https://doi.org/10.1016/j.jhazmat.2007.11.048>
- Tatawat, R. K., & Chandel, C. P. S. (2008). A hydrochemical profile for assessing the groundwater quality of Jaipur City. *Environmental Monitoring and Assessment*, 143, 337–343. <https://doi.org/10.1007/s10661-007-9936-3>
- Torres-Gómez, N., Nava, O., Argueta-Figueroa, L., García-Contreras, R., Baeza-Barrera, A., & Vilchis-Nestor, A. R. (2019). Shape tuning of magnetite nanoparticles obtained by hydrothermal synthesis: Effect of temperature. *Journal of Nanomaterials*. <https://doi.org/10.1155/2019/7921273>
- Tran, H. N., You, S. J., Hosseini-Bandegharai, A., & Chao, H. P. (2017). Mistakes and inconsistencies regarding adsorption of contaminants from aqueous solutions: A critical review. *Water Research*, 120, 88–116. <https://doi.org/10.1016/j.watres.2017.04.014>
- World Health Organization. (2011). *Guidelines for Drinking-water Quality*. World Health Organization.
- WWAP, P. M. de E., & de los R. H. de la U. (2019). *Informe Mundial de las Naciones Unidas sobre el Desarrollo de los Recursos Hídricos 2019: No dejar a nadie atrás*. Paris : UNESCO, 2019. <https://unesdoc.unesco.org/ark:/48223/pf0000367304>
- Yang, L., Wei, Z., Zhong, W., Cui, J., & Wei, W. (2016a). Modifying hydroxyapatite nanoparticles with humic acid for highly efficient removal of Cu(II) from aqueous solution. *Colloids and Surfaces a: Physicochemical and Engineering Aspects*, 490, 9–21. <https://doi.org/10.1016/j.colsurfa.2015.11.039>
- Yang, Z., Fang, Z., Zheng, L., Cheng, W., Tsang, P. E., Fang, J., & Zhao, D. (2016b). Remediation of lead contaminated soil by biochar-supported nano-hydroxyapatite. *Ecotoxicology and Environmental Safety*, 132, 224–230. <https://doi.org/10.1016/j.ecoenv.2016.06.008>
- Yang, Z., Gong, H., He, F., Repo, E., Yang, W., Liao, Q., & Zhao, F. (2022). Iron-doped hydroxyapatite for the simultaneous remediation of lead-, cadmium- and arsenic-contaminated soil. *Environmental Pollution*, 312, 119953. <https://doi.org/10.1016/j.envpol.2022.119953>
- Zeng, Y., Wang, K., Yao, J., & Wang, H. (2014). Hollow carbon beads for significant water evaporation enhancement. *Chemical Engineering Science*, 116, 704–709. <https://doi.org/10.1016/j.ces.2014.05.057>
- Zhang, W., Wang, F., Wang, P., Lin, L., Zhao, Y., Zou, P., Zhao, M., Chen, H., Liu, Y., & Zhang, Y. (2016). Facile synthesis of hydroxyapatite/yeast biomass composites and their adsorption behaviors for lead (II). *Journal of Colloid and Interface Science*, 477, 181–190. <https://doi.org/10.1016/j.jcis.2016.05.050>
- Zheltova, V., Vlasova, A., Bobrysheva, N., Abdullin, I., Semenov, V., Osmolowsky, M., Voznesenskiy, M., & Osmolovskaya, O. (2020). Fe₃O₄@HAP core-shell nanoparticles as MRI contrast agent: Synthesis, characterization and theoretical and experimental study of shell impact on magnetic properties. *Applied Surface Science*, 531, 147352. <https://doi.org/10.1016/j.apsusc.2020.147352>

Publisher's Note Springer Nature remains neutral with regard to jurisdictional claims in published maps and institutional affiliations.

Springer Nature or its licensor (e.g. a society or other partner) holds exclusive rights to this article under a publishing agreement with the author(s) or other rightsholder(s); author self-archiving of the accepted manuscript version of this article is solely governed by the terms of such publishing agreement and applicable law.